THE JOURNAL OF PHYSICAL CHEMISTRY C
A JOURNAL OF THE AMERICAN CHEMICAL SOCIETY

pubs.acs.org/JPCC
Article

Endohedral Two-Dimensional Fullerene Networks: A First-Principles Study of Electronic and Optical Properties

Marcelo L. Pereira Junior, Raphael M. Tromer, Luiz A. Ribeiro Junior, and Douglas S. Galvão*

Cite This: J. Phys. Chem. C 2026, 130, 7900−7908
Read Online
ACCESS | Metrics & More | Article Recommendations

ABSTRACT: The quasi-hexagonal phase of the two-dimensional fullerene network ($qHPC_{60}$), recently synthesized, has emerged as a stable carbon-based material with distinct structural and electronic features. In this work, we employed density functional theory (DFT) calculations within the PBE functional to investigate the electronic and optical properties of its endohedral derivatives. The encapsulation of nitrogen, cerium, and strontium atoms inside fullerene cages was systematically analyzed at different concentrations. Our results show that nitrogen encapsulation preserves the semiconducting character of pristine $qHPC_{60}$ and introduces localized intragap states with potential relevance for discrete optical emission, whereas cerium and strontium encapsulation induces a metallic behavior associated with intraband states near the conduction edge. These modifications induce a red shift of the absorption onset into the visible spectrum, accompanied by enhanced refractive and absorptive responses. The main electronic features identified at full encapsulation are preserved at intermediate fillings, with Ce and Sr reverting to a semiconducting behavior at the lowest filling examined. Overall, the findings highlight impurity-endowed $qHPC_{60}$ as a promising platform for optoelectronic and light-harvesting applications.

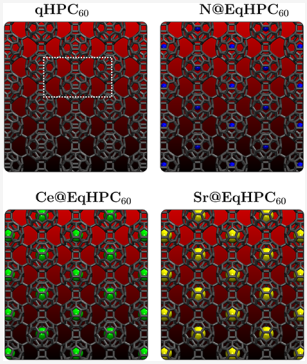

INTRODUCTION

Carbon-based two-dimensional (2D) materials have been extensively investigated due to their mechanical, optical, and electronic properties.[1−3] In general, they exhibit high mechanical and thermal stability, good electron mobility, and optical transparency, which make them promising candidates for the development of optoelectronic devices.[4−11]

Among the already synthesized structures, graphene is one of the most important (together with fullerenes and nanotubes), combining high electrical conductivity, mechanical robustness, and broad applicability in different technological contexts.[12,13] Its discovery and impact stimulated the search for other 2D carbon allotropes with complementary properties and the potential to overcome some of graphene's limitations. Within this effort, it is worth mentioning the synthesis of biphenylene network (BPN),[4,14] γ-graphyne (γ-GY),[15−18] and monolayer amorphous carbon (MAC).[11,19,20] More recently, C_{60} fullerene monolayers ($2DC_{60}$)[21−28] have attracted much interest because they present a topology that combines closed and open cage-like motifs, sometimes described as 2.5-dimensional materials. This configuration is particularly suitable for applications such as encapsulation, gas capture, lithium storage, catalysis, and lubrication.[29−36]

Recent studies have investigated the fundamental properties of $2DC_{60}$. These include anisotropic thermal expansion associated with different types of intermolecular bonding,[37] the effect of strain engineering on thermoelectric performance,[38] interfacial thermal conductance in graphene/$qHPC_{60}$ heterostructures,[39] charge transport mediated by large polarons and strongly influenced by lattice anisotropy,[40] and hydrogen storage capacity.[41] These investigations confirm that $2DC_{60}$ represents a stable and versatile platform with potential for a wide range of technological applications.

Endohedral fullerenes (endofullerenes) form another very important class of fullerene derivatives, in which atoms or small molecules are encapsulated inside the C_{60} or larger fullerenes.[42−45] Encapsulation can significantly alter the electronic, optical, and magnetic properties of the system.[46−48] Several synthesis routes have been reported for endofullerenes, including chemical reactions,[49] high-pressure techniques,[50] and solid-state methods.[51]

Recently, Baldoví et al. reported the theoretical realization of graphendofullerenes, 2D networks composed of covalently bonded endohedral C_{80} units encapsulating V_3N clusters.[52] Their results revealed an interesting magnetic response arising from the interaction between the encapsulated clusters and the extended C_{80} framework, demonstrating that the host−guest coupling can significantly modify the collective electronic behavior of 2D carbon systems. Concerning C_{60} units, which constitute the fundamental building blocks of recently

Received: April 21, 2026
Revised: May 18, 2026
Accepted: May 19, 2026
Published: May 22, 2026

https://doi.org/10.1021/acs.jpcc.6c02579
J. Phys. Chem. C 2026, 130, 7900−7908

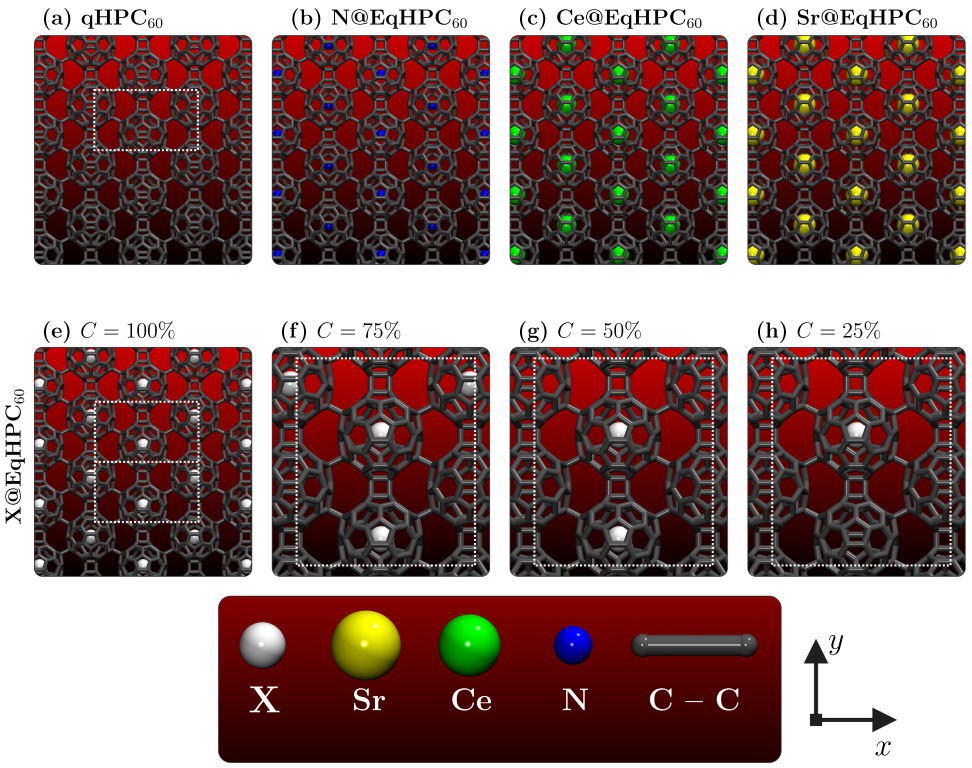

Figure 1. Structures of $qHPC_{60}$ and endohedral variations. Pristine $qHPC_{60}$ (a), encapsulation with N (b), Ce (c), and Sr (d), and encapsulation fractions of 100% (e), 75% (f), 50% (g), and 25% (h). Here, X denotes a generic encapsulated atom (N, Ce, or Sr).

synthesized 2D fullerene materials,[21] Zhao and collaborators investigated, through Density Functional Theory (DFT) calculations, endohedral $qHPC_{60}$ systems modified by C_{60} units encapsulating uranium and thorium dimers (U_2 and Th_2). They identified the formation of single bonds between the encapsulated metal atoms and magnetic properties induced by the fullerene confinement.[53] Nevertheless, although significant progress has been achieved in the synthesis and characterization of the $2DC_{60}$ system, as well as in the study of endofullerenes in isolated cages and van der Waals solids, the investigation of endofullerenes in two-dimensional C_{60} networks remains largely unexplored. Understanding how encapsulated species influence the electronic and optical properties of these 2D architectures is crucial for advancing their applications in energy-related, catalytic, and optoelectronic fields.

In this work, we have carried out a comprehensive DFT-based investigation on the electronic and optical properties of endofullerene derivatives based on the closely packed quasi-hexagonal C_{60} monolayer ($EqHPC_{60}$) phase. We have considered the encapsulation of nitrogen (N), strontium (Sr), and cerium (Ce) atoms, which have previously been studied in van der Waals crystals formed by C_{60}.[54−58] The results reveal semiconducting electronic band gaps with localized states for N-encapsulation, as well as a metallic behavior for Ce and Sr.

METHODS

As mentioned above, we have considered the quasi-hexagonal phase of C_{60} ($qHPC_{60}$), which has been identified as the most stable configuration for $2DC_{60}$.[22] This phase is described by a rectangular unit cell containing 120 carbon atoms, corresponding to two C_{60} molecules, as illustrated in Figure 1a. From this pristine cell, endohedral systems were generated by placing one atom of N, Ce, and Sr inside each C_{60} cage, Figure 1b−d. When both cages of the unit cell were filled, the fully encapsulated configuration with 100% concentration was obtained, as schematically depicted in Figure 1e. To explore other concentrations, a $1 \times 2 \times 1$ supercell, containing four C_{60} molecules, was created.

We have considered five cases, all encapsulated fullerenes, removing one, two, and three atomic species to obtain filling concentrations of 75% (Figure 1f), 50% (Figure 1g), and 25% (Figure 1h), respectively. Figure 1 summarizes the setup of the investigated systems, from the pristine structure to different degrees of filling of the C_{60} cages.

All structures were fully optimized (atomic positions and lattice parameters) prior to the electronic and optical analyses. Structural relaxations and property calculations were performed within DFT, including van der Waals corrections,[59−61] as implemented in the SIESTA code.[62] Localized basis functions with a single-ζ (SZ) set were employed. This choice was dictated by the size of the systems considered (120 to 240 atoms per cell) and by the cost associated with the lanthanide 4*f* states in $Ce@EqHPC_{60}$. While polarized bases refine the absolute values of bandgaps and lattice parameters, the qualitative features supporting the present conclusions, namely the position of the impurity-derived levels and the semiconductor-to-metal transition driven by Ce and Sr, are not expected to be altered by basis truncation. Spin−orbit coupling was likewise omitted, since N is a light atom, the Sr 5s states form a closed shell, and the Ce 4f states are nearly dispersionless and lie above the Fermi level, so that the semiconductor-to-metal transition reported here is governed by Ce−C and Sr−C hybridization rather than by fine-structure splitting. The obtained lattice parameters, electronic band structures, and optical properties were found to be consistent with previous investigations of $qHPC_{60}$,[22] validating the methodology.

For lanthanide atoms such as cerium, the presence of 4f orbitals leads to a large number of degenerate states near the Fermi level, which sometimes makes the convergence of the self-consistent field (SCF) cycle difficult. To address this difficulty, thermal smearing was applied.[63] Exchange-correlation effects were described within the generalized gradient approximation (GGA) using the Perdew−

https://doi.org/10.1021/acs.jpcc.6c02579
J. Phys. Chem. C 2026, 130, 7900−7908

Burke−Ernzerhof (PBE) functional.[64,65] Core electrons were treated with norm-conserving Troullier-Martins pseudopotentials.[66]

Convergence tests were performed for the energy cutoff, k-point mesh, and vacuum spacing. Based on these tests, an energy cutoff of 200 Ry, a Monkhorst−Pack 5 × 5 × 1 k-point grid, and a vacuum spacing of 30 Å along the z-direction were adopted to prevent spurious interactions between periodic (mirror) images. Atomic positions and in-plane lattice vectors (x and y) were fully relaxed, while the out-of-plane vector (z) was kept fixed. The convergence criterion for maximum forces in each atom was set to 0.05 eV/Å. Both the unit cell and the 1 × 2 × 1 supercell used to access partial fillings were independently optimized, and the fully encapsulated limit obtained in each yielded consistent structural and electronic results, confirming the adequacy of the periodic representations adopted. The thermodynamic stability of the endohedral configurations is supported by the cohesive and formation energies discussed below, while the dynamical and thermal stability of the pristine $qHPC_{60}$ scaffold has been characterized in previous theoretical studies.[23−25]

The electronic band structure was calculated along the high-symmetry path of the rectangular Brillouin zone defined as Γ = (0.0, 0.0) to X = (0.5, 0.0), U = (0.5, 0.5), Y = (0.0, 0.5), and back to Γ = (0.0, 0.0). An external electric field of 1.0 V/Å was applied along three polarization planes to estimate the optical coefficients.[67] The optical coefficients were extracted from the complex dielectric function, where the imaginary part was obtained using Fermi's golden rule[68] and the real part from the Kramers−Kronig relation.[69] From these functions, we calculated the absorption coefficient α according to

$$\alpha(\omega) = \sqrt{2}\,\omega[(\epsilon_1^2(\omega) + \epsilon_2^2(\omega))^{1/2} - \epsilon_1(\omega)]^{1/2} \quad (1)$$

the refractive index η using

$$\eta(\omega) = \frac{1}{\sqrt{2}}[(\epsilon_1^2(\omega) + \epsilon_2^2(\omega))^{1/2} + \epsilon_1(\omega)]^2 \quad (2)$$

and the reflectivity R given by

$$R(\omega) = \left[\frac{(\epsilon_1(\omega) + i\epsilon_2(\omega))^{1/2} - 1}{(\epsilon_1(\omega) + i\epsilon_2(\omega))^{1/2} + 1}\right]^2 \quad (3)$$

RESULTS AND DISCUSSION

The initial analysis focuses on the structural and energetic aspects of the investigated systems. Table 1 summarizes the lattice parameters, cohesive energies (E_{cohe}), formation energies (E_{form}), and the charge accumulated in the C_{60} units for the pristine $qHPC_{60}$ and for the endohedral configurations containing N, Ce, and Sr, hereafter denoted as N@$EqHPC_{60}$, Ce@$EqHPC_{60}$, and Sr@$EqHPC_{60}$.

Table 1. Structural Parameters Including Cohesive Energy (E_{cohe}), Formation Energy (E_{form}), Charge at the C_{60} Units, and Lattice Vectors (a and b)

structure	E_{cohe} (eV/atom)	E_{form} (meV/atom)	$Q_{qHPC_{60}}$ (e)	a (Å)	b (Å)
$qHPC_{60}$	−7.10			16.04	9.26
N@ $EqHPC_{60}$	−7.02	−40.79	+0.001	16.35	9.47
Ce@ $EqHPC_{60}$	−7.17	−178.13	+0.033	16.36	9.48
Sr@ $EqHPC_{60}$	−7.13	−145.18	+0.032	16.35	9.47

The E_{cohe} was obtained using the following expression:

$$E_{cohe} = \frac{E_{X@EqHPC_{60}} - N_C E_C - N_X E_X}{N_C + N_X} \quad (4)$$

where $E_{X@EqHPC_{60}}$, E_C, and E_X represent the total energy of the X@$EqHPC_{60}$ system, and the energies of isolated C and X atoms, respectively, with X = Sr, Ce, or N. N_C and N_X correspond to the number of carbon and endohedral atoms in the system. The calculated E_{cohe} values indicate that all endohedral configurations remain stable with respect to the pristine $qHPC_{60}$ structure. The E_{form} was computed as

$$E_{form} = E_{X@EqHPC_{60}} - E_{qHPC_{60}} - N_X E_X \quad (5)$$

where $E_{qHPC_{60}}$ is the total energy of the pristine $qHPC_{60}$ system, and the remaining terms are defined as above. A consistent trend is observed between E_{cohe} and E_{form}, such that more negative formation energies correspond to more stable configurations. Within this framework, Ce@$EqHPC_{60}$ emerges as the most stable case, showing the smallest values for both quantities.

No significant transfer charges were observed. The larger values for Sr and Ce can be attributed to the differences in atomic radii and cage interactions. Sr (2.15 Å) and Ce (1.81 Å) are considerably larger than N (0.65 Å), which brings them closer to the cage walls and increases the electrostatic coupling. Their more negative E_{form} values also reinforce the stronger interaction with the host lattice. The lattice vectors a and b exhibit a slight expansion compared to the pristine configuration and are basically the same for all encapsulated cases. The angle values remain essentially at 90°, confirming that encapsulation preserves the underlying lattice symmetry.

The electronic band structures for the pristine and endohedral systems are shown in Figure 2, which includes $qHPC_{60}$ as well as the encapsulated configurations N@$EqHPC_{60}$, Ce@$EqHPC_{60}$, and Sr@$EqHPC_{60}$.

As a reference, pristine $qHPC_{60}$ displays a direct electronic bandgap at the Γ point of approximately 0.86 eV, in agreement with previous reports, with the valence and conduction bands dominated by C_{2p} orbitals. This configuration serves as the baseline for evaluating the modifications introduced by encapsulation.

For N@$EqHPC_{60}$ (see Figure 2b), a localized level emerges within the gap, associated with N_{2p} orbitals. This intragap state reduces the effective bandgap to approximately 0.46 eV, introduces additional recombination channels, and indicates a localized regime compatible with discrete emission. There is a conceptual parallel with wide-bandgap semiconductors such as hBN, where localized states have been identified as the origin of single-photon emission (SPE) at room temperature.[70] Although confirmation of such behavior in $qHPC_{60}$ requires further investigation, this result suggests potential applications in optical and quantum information.

Figure 2c shows the case of Ce@$EqHPC_{60}$, which exhibits a nearly flat state in the conduction region, located approximately 1 eV above the Fermi level, predominantly of Ce_{4f} character, with noticeable hybridization with C_{2p} states. This feature reflects the charge transfer from the encapsulated atom to the carbon cage and is consistent with the more negative formation energy observed for the Ce-containing system. As a consequence, the material displays a metallic character, with the Fermi level crossing the conduction band. These properties indicate a strong electronic coupling between the encapsulated atom and the fullerene cage, which may influence charge transport mechanisms and enable additional optical transitions near the conduction band edge.

https://doi.org/10.1021/acs.jpcc.6c02579
J. Phys. Chem. C 2026, 130, 7900−7908

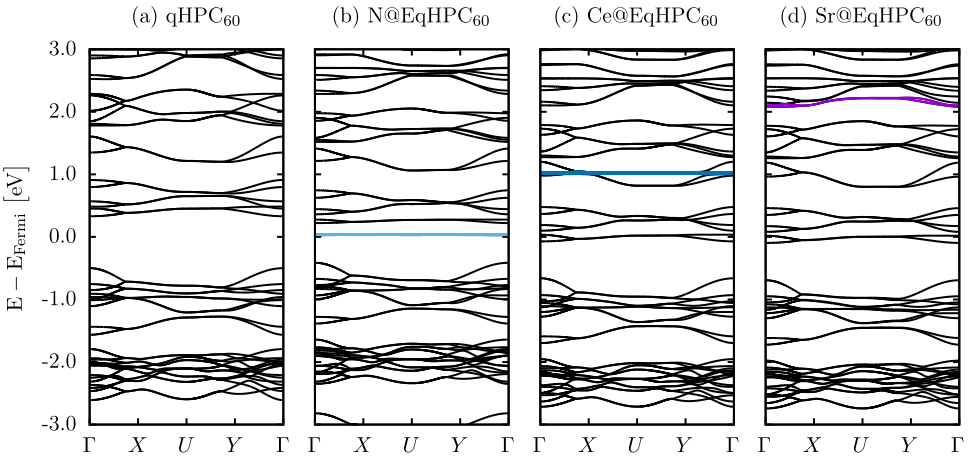

Figure 2. Electronic band structures for pristine $qHPC_{60}$ (a), $N@EqHPC_{60}$ (b), $Ce@EqHPC_{60}$ (c), and $Sr@EqHPC_{60}$ (d).

A similar behavior is observed in Figure 2d for $Sr@EqHPC_{60}$, where a nearly flat state associated with Sr_{5s} orbitals appears approximately 2.1 eV above the Fermi level. This state exhibits slightly higher dispersion compared to that observed for the $Ce@EqHPC_{60}$ system, indicating a lower degree of localization, yet still sufficient to modify the conduction band profile. The crossing of the Fermi level with the conduction band confirms the metallic character of the system, reinforcing the role of the interaction between the encapsulated atom and the carbon cage in defining the electronic behavior. The correlation between charge transfer and formation energy, which is less pronounced in the case of N, further highlights the combined influence of the atomic radius and electrostatic interaction discussed in the structural analysis.

Taken together with the band-structure analysis, Figure 3 consolidates the electronic trends by displaying the Density of States (DOS) for the pristine and endohedral 2D systems, all aligned to $E_F = 0$ eV. The pristine system exhibits a clear gap, whereas nitrogen introduces a sharp localized level inside the gap, consistent with the flat midgap band discussed earlier.

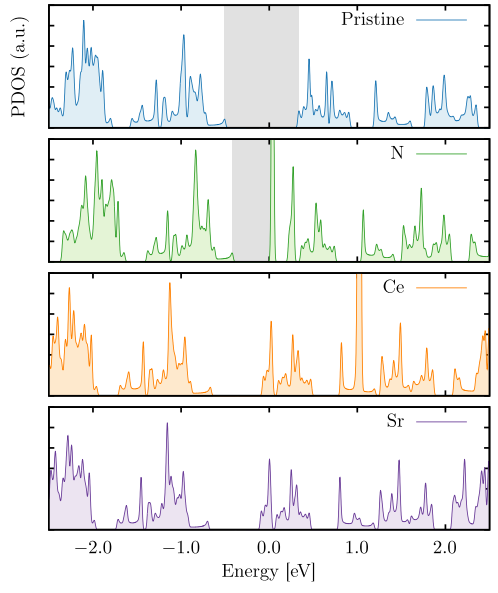

Figure 3. Electronic densities of states for pristine $qHPC_{60}$, $N@EqHPC_{60}$, $Ce@EqHPC_{60}$, and $Sr@EqHPC_{60}$. Energies are aligned to $E_F = 0$. The shaded region indicates the bandgap.

Cerium and strontium produce intense features just above E_F that originate from Ce_{4f} and Sr_{5s} states and are coherent with the weakly dispersive conduction bands near the Fermi level. These impurity-derived states are expected to alter the optical response by enabling additional transitions from the valence-band maximum (VBM) to intragap levels and from the VBM to intraband states near the conduction-band minimum (CBM). The concentration dependence of these features is examined next, followed by a quantitative analysis of the derived optical coefficients.

In Figure 4, the electronic band structures of $N@EqHPC_{60}$, $Ce@EqHPC_{60}$, and $Sr@EqHPC_{60}$ are presented for filling concentrations of 75% (Figure 1f), 50% (Figure 1g), and 25% (Figure 1h).

The results show that the main features of the $EqHPC_{60}$ band structure are preserved under partial encapsulation, confirming the structural and electronic stability of the carbon framework. The band dispersion remains nearly unchanged relative to the filled systems, with the differences limited to the intensity and energetic position of the localized states introduced by the encapsulated atoms.

For $N@EqHPC_{60}$, shown in Figure 4a–c, the systems remain semiconducting at all filling levels. The N_{2p}-derived intragap states appear consistently within the same energy range and maintain their separation from the band edges. The reduction in filling concentration only decreases their spectral intensity, without modifying the overall electronic character.

For $Ce@EqHPC_{60}$, shown in Figure 4d–f, nearly flat Ce_{4f} states persist near the Fermi level. At 75 and 50% fillings, these states overlap with the conduction band, producing metallic behavior comparable to that of the fully encapsulated case. At 25%, the system becomes semiconducting, with midgap states into the conduction band and a bandgap of approximately 0.44 eV.

A similar trend is observed for $Sr@EqHPC_{60}$ in Figure 4g–i. For 75 and 50% fillings, Sr_{5s} states intersect the valence band, resulting in metallic behavior. At 25%, the system exhibits an electronic bandgap of approximately 0.18 eV, with midgap states located in the valence band. The decrease in Sr concentration weakens hybridization between Sr and the carbon framework, thereby increasing electronic localization.

The optical response of pristine $qHPC_{60}$ and their investigated endostructures is summarized in Figure 5, which presents the simulated absorption spectra (α), refractive index

https://doi.org/10.1021/acs.jpcc.6c02579
J. Phys. Chem. C 2026, 130, 7900−7908

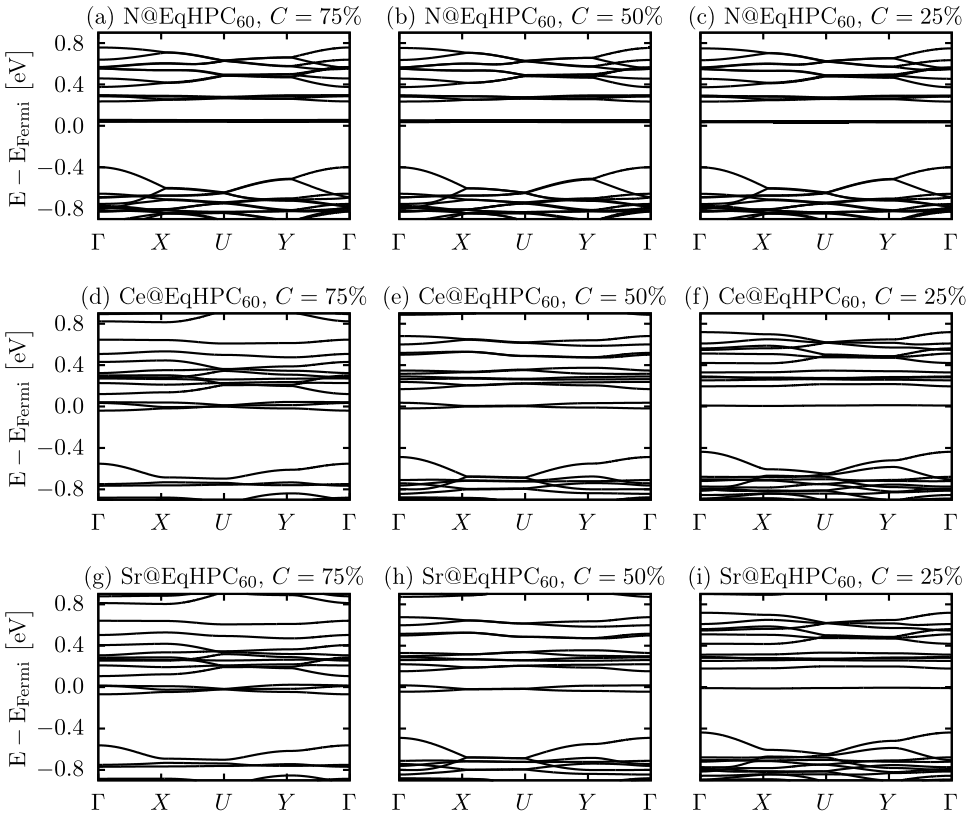

Figure 4. Electronic band structures of endohedral $qHPC_{60}$ systems at different filling concentrations. Panels (a–c) correspond to $N@EqHPC_{60}$, (d–f) to $Ce@EqHPC_{60}$, and (g–i) to $Sr@EqHPC_{60}$, with filling values of 75, 50, and 25%, respectively.

(η), and the reflectivity (R) as a function of photon energy for the three light polarizations directions E||X, E||Y, and E||Z.

For the pristine case, shown in Figure 5a,e,i, the optical response is markedly anisotropic across the three polarization directions. The first absorption peak is located around 2.6 eV for E||X and E||Z, within the blue region of the visible spectrum. For E||Y, it is shifted to the ultraviolet region near 3.5 eV. This transition is associated with the excitation between the highest occupied crystalline orbital (HOCO) and the lowest unoccupied crystalline orbital (LUCO). Subsequent peaks lie in the ultraviolet region, consistent with typical carbon-based optical responses.[71]

For the endofilled systems, illustrated in Figure 5b–d, the first absorption peaks are red-shifted compared to the pristine case, and all fall within the visible range. For E||X and E||Z, the initial transitions occur around 2.2 eV, corresponding to the green region, while for E||Y the first peak appears near 3.1 eV, within the violet region. These features are consistent with the presence of localized electronic states created by the encapsulated atoms, as identified in the band structure analysis.

The optical bandgap values were obtained from the Tauc plots derived from the calculated absorption coefficients along the three polarization directions (E||X, E||Y, and E||Z). In this approach, the absorption coefficient α is related to the photon energy ($h\nu$) according to the expression:

$$(\alpha h\nu)^2 = A(h\nu - E_g^{opt}) \tag{6}$$

where A is a proportionality constant and E_g^{opt} is the optical bandgap energy. The linear portion of the plot of $(\alpha h\nu)^2$ versus $h\nu$ was extrapolated to intercept the energy axis, yielding the value of E_g^{opt}. This method assumes a direct allowed electronic transition, which is appropriate for materials exhibiting strong optical absorption near the band edge.

For the pristine $EqHPC_{60}$, the extracted optical gap is approximately 0.78 eV, in close agreement with the electronic bandgap obtained from the band structure calculations. This result confirms the consistency between the electronic and optical descriptions and indicates that excitonic effects play a minor role in this system. In contrast, for the $N@EqHPC_{60}$ system, the optical bandgap decreases to about 0.48 eV, reflecting the influence of the nitrogen-induced midgap states. This decrease in the optical transition threshold corroborates the presence of localized states within the electronic gap and confirms that nitrogen encapsulation effectively narrows the bandgap by introducing additional electronic levels near the Fermi energy.

The reflectivity spectra, shown in Figure 5i–l, also confirm the spectral shifts induced by encapsulation. In pristine $qHPC_{60}$, the reflectivity peaks occur at 2.7 eV for E||X and E||Z and at 3.1 eV for E||Y. In the endofilled systems, these peaks shift to lower energies, with maxima at approximately 2.2 eV (green region) and 2.7 eV (blue region). Within the visible spectrum, reflectivity reaches about 10% for pristine $qHPC_{60}$ and $N@EqHPC_{60}$, while for $Ce@EqHPC_{60}$ and $Sr@EqHPC_{60}$ it decreases to around 7.5%. These findings indicate that endohedral $qHPC_{60}$ systems exhibit low reflectivity and refractive indices greater than unity, which favors the efficient absorption of visible photons, particularly in the green, blue, and yellow regions.

In Figure 6, we present a schematic diagram of the spatial localization of the HOCO and LUCO frontier crystalline orbitals for all investigated systems. In general, these orbitals are distributed along the C–C bonds, forming favorable

https://doi.org/10.1021/acs.jpcc.6c02579
J. Phys. Chem. C 2026, 130, 7900–7908

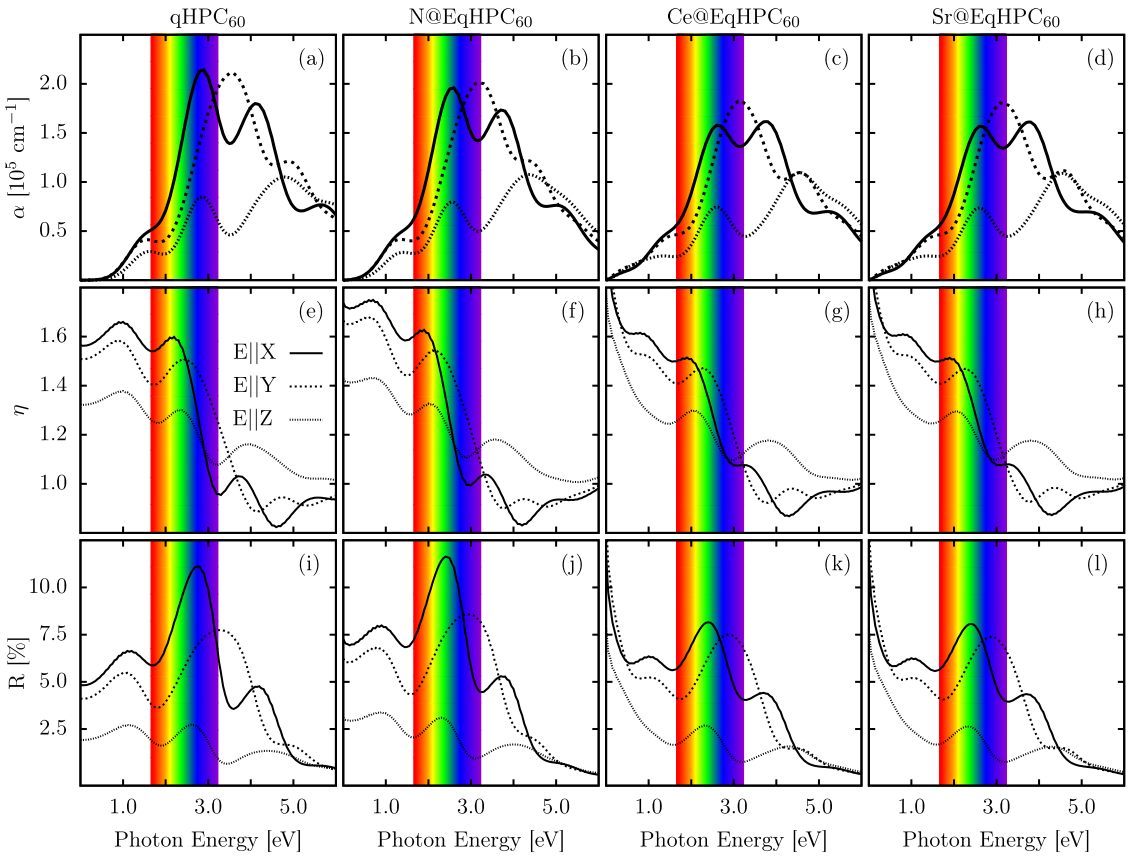

Figure 5. Simulated absorption spectra (α), refractive index (η), and reflectivity (R) as a function of photon energy for pristine qHPC$_{60}$ (a, e, i), N@EqHPC$_{60}$ (b, f, j), Ce@EqHPC$_{60}$ (c, g, k), and Sr@EqHPC$_{60}$ (d, h, l). Solid, dashed, and dotted lines correspond to E||X, E||Y, and E||Z polarization directions, respectively. Colored bands indicate the visible spectrum range.

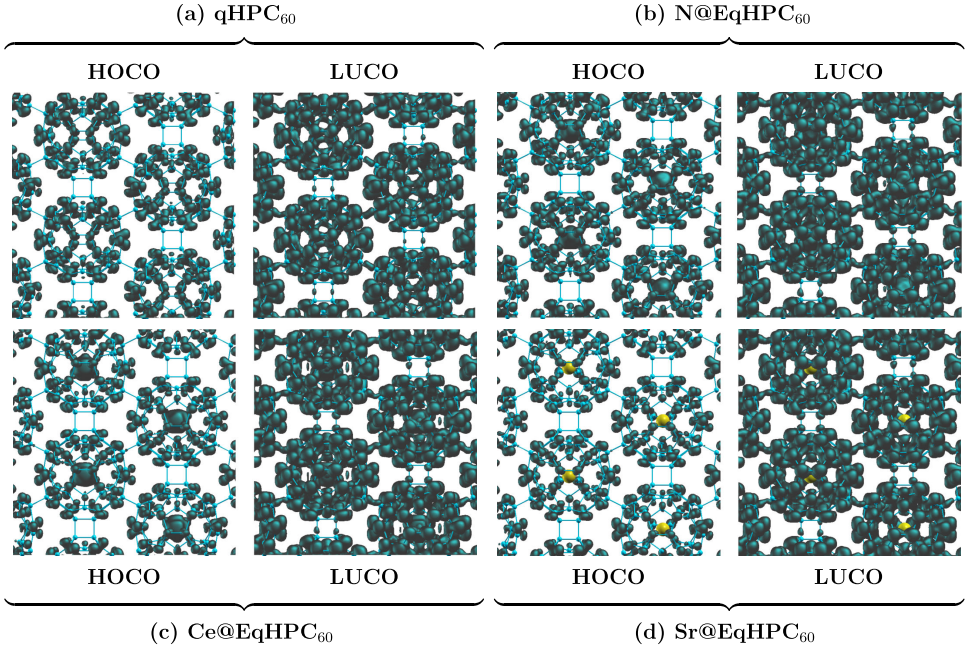

Figure 6. Spatial distribution of the HOCO (left) and LUCO (right) frontier crystalline orbitals for pristine qHPC$_{60}$ (a), N@EqHPC$_{60}$ (b), Ce@EqHPC$_{60}$ (c), and Sr@EqHPC$_{60}$ (d). In the color scheme, dark green indicates regions of high electron localization, and cyan corresponds to the carbon atoms and C−C bonds.

pathways for electron transport and thereby supporting high charge mobility. In the pristine system, Figure 6a, the HOCO is mainly localized within the internal C−C bonds of the C$_{60}$ units, while the LUCO, which governs electronic mobility, is more uniformly distributed across the interunit bonds. A similar behavior is observed for Sr@EqHPC$_{60}$, Figure 6d,

https://doi.org/10.1021/acs.jpcc.6c02579
J. Phys. Chem. C 2026, 130, 7900−7908

where delocalization over the bonds remains predominant. In contrast, both HOCO and LUCO for N@EqHPC$_{60}$, Figure 6b, and Ce@EqHPC$_{60}$, Figure 6c, exhibit strong localization on the encapsulated atoms. These electronic states originate primarily from 2p electrons, and their localization is consistent with the reduced bandgap discussed earlier, since high charge delocalization favors a smaller separation between the frontier levels.

CONCLUSIONS

We have performed a systematic investigation of the electronic and optical properties of endohedral fullerene networks based on the quasi-hexagonal phase of C$_{60}$. Using density functional theory, we examined pristine qHPC$_{60}$ and its endohedral variants with nitrogen, cerium, and strontium at different encapsulation concentrations. The results reveal that nitrogen encapsulation preserves the semiconducting character of the pristine system through localized intragap states, whereas cerium and strontium encapsulation induces a metallic behavior associated with intraband states near the conduction band minimum. These impurity-derived states modify the optical absorption profile and shift the first absorption peak into the visible region. The refractive index and reflectivity spectra further demonstrate anisotropic responses, with reduced reflectivity in the visible range, favoring efficient photon absorption. The analysis of frontier orbitals confirms that charge transport pathways are generally preserved, with impurity localization modulating the magnitude of the electronic bandgap. The concentration study indicates that the main electronic features identified at full encapsulation are preserved at intermediate fillings, with a reversion to semiconducting behavior emerging at the lowest filling fraction examined for the cerium and strontium cases. Taken together, these findings establish impurity-endowed qHPC$_{60}$ as a versatile candidate for applications in optoelectronics, light-harvesting, and potentially quantum information technologies.

AUTHOR INFORMATION

Corresponding Author

Douglas S. Galvão − *Department of Applied Physics, State University of Campinas, 13083-970 Campinas, São Paulo, Brazil;* orcid.org/0000-0003-0145-8358; Email: galvao@ifi.unicamp.br

Authors

Marcelo L. Pereira Junior − *Department of Electrical Engineering, College of Technology, University of Brasília, 70910-900 Brasília, Federal District, Brazil; Department of Materials Science and NanoEngineering, Rice University, Houston, Texas 77005, United States;* orcid.org/0000-0001-9058-510X

Raphael M. Tromer − *Institute of Physics, University of Brasília, 70910-900 Brasília, Federal District, Brazil;* orcid.org/0000-0002-6180-5641

Luiz A. Ribeiro Junior − *Institute of Physics, University of Brasília, 70910-900 Brasília, Federal District, Brazil; Computational Materials Laboratory, University of Brasília, 70910-900 Brasília, Federal District, Brazil;* orcid.org/0000-0001-7468-2946

Complete contact information is available at: https://pubs.acs.org/10.1021/acs.jpcc.6c02579

Funding

The Article Processing Charge for the publication of this research was funded by the Coordenacao de Aperfeicoamento de Pessoal de Nivel Superior (CAPES), Brazil (ROR identifier: 00x0ma614).

Notes

The authors declare no competing financial interest.

ACKNOWLEDGMENTS

M.L.P.J. acknowledges financial support from FAPDF (grant 00193-00001807/2023-16), CNPq (grants 444921/2024-9 and 308222/2025-3), and CAPES (grant 88887.005164/2024-00). Computational resources were provided by the National High-Performance Computing Center in São Paulo (CENAPAD-SP, UNICAMP, projects proj931 and proj960) and the High-Performance Computing Center (NACAD, Lobo Carneiro Supercomputer, UFRJ, project a22002). L.A.R.J. acknowledges the financial support from FAP-DF grants 00193.00001808/2022-71 and 00193-00001857/2023-95, FAPDF-PRONEM grant 00193.00001247/2021-20, CNPq grants 350176/2022-1, 167745/2023-9, 444111/2024-7, and PDPG-FAPDF-CAPES Centro-Oeste 00193-00000867/2024-94. We thank the Coaraci Supercomputer Center for computer time (FAPESP grant #2019/17874-0) and the Center for Computing in Engineering and Sciences at Unicamp (FAPESP grant #2013/08293-7). D.S.G. also acknowledges support from INEO/CNPq and FAPESP grant 2025/27044-5. The authors also thank Colin P. Nuckolls (Columbia University) for valuable discussions and suggestions that contributed to this research.

REFERENCES

(1) Gao, L. Flexible device applications of 2D semiconductors. *Small* **2017**, *13*, No. 1603994.

(2) Zhang, R.-S.; Jiang, J.-W. The art of designing carbon allotropes. *Front. Phys.* **2019**, *14*, No. 13401.

(3) Glavin, N. R.; Rao, R.; Varshney, V.; Bianco, E.; Apte, A.; Roy, A.; Ringe, E.; Ajayan, P. M. Emerging applications of elemental 2D materials. *Adv. Mater.* **2020**, *32*, No. 1904302.

(4) Fan, Q.; Yan, L.; Tripp, M. W.; Krejčí, O.; Dimosthenous, S.; Kachel, S. R.; Chen, M.; Foster, A. S.; Koert, U.; Liljeroth, P.; Gottfried, J. M. Biphenylene network: A nonbenzenoid carbon allotrope. *Science* **2021**, *372*, 852−856.

(5) Berber, S.; Osawa, E.; Tománek, D. Rigid crystalline phases of polymerized fullerenes. *Phys. Rev. B* **2004**, *70*, No. 085417.

(6) Alsayoud, A. Q.; Manga, V. R.; Muralidharan, K.; Vita, J.; Bringuier, S.; Runge, K.; Deymier, P. Atomistic insights into the effect of polymerization on the thermophysical properties of 2-D C60 molecular solids. *Carbon* **2018**, *133*, 267−274.

(7) Wang, Z.; Zhou, X.-F.; Zhang, X.; Zhu, Q.; Dong, H.; Zhao, M.; Oganov, A. R. Phagraphene: a low-energy graphene allotrope composed of 5−6−7 carbon rings with distorted dirac cones. *Nano Lett.* **2015**, *15*, 6182−6186.

(8) Wang, S.; Yang, B.; Chen, H.; Ruckenstein, E. Popgraphene: a new 2D planar carbon allotrope composed of 5−8−5 carbon rings for high-performance lithium-ion battery anodes from bottom-up programming. *J. Mater. Chem. A* **2018**, *6*, 6815−6821.

(9) Zhuo, Z.; Wu, X.; Yang, J. Me-graphene: a graphene allotrope with near zero Poisson's ratio, sizeable band gap, and high carrier mobility. *Nanoscale* **2020**, *12*, 19359−19366.

(10) Karaush, N. N.; Baryshnikov, G. V.; Minaev, B. F. DFT characterization of a new possible graphene allotrope. *Chem. Phys. Lett.* **2014**, *612*, 229−233.

(11) Toh, C.-T.; Zhang, H.; Lin, J.; Mayorov, A. S.; Wang, Y.-P.; Orofeo, C. M.; Ferry, D. B.; Andersen, H.; Kakenov, N.; Guo, Z.;

Abidi, I. H.; Sims, H.; Suenaga, K.; Pantelides, S. T.; Özyilmaz, B. Synthesis and properties of free-standing monolayer amorphous carbon. *Nature* **2020**, *577*, 199−203.
(12) Novoselov, K. S.; Geim, A. K.; Morozov, S. V.; Jiang, D.-e.; Zhang, Y.; Dubonos, S. V.; Grigorieva, I. V.; Firsov, A. A. Electric field effect in atomically thin carbon films. *Science* **2004**, *306*, 666−669.
(13) Novoselov, K. S. Nobel lecture: Graphene: Materials in the flatland. *Rev. Mod. Phys.* **2011**, *83*, 837.
(14) Pereira, M. L.; da Cunha, W.; de Sousa, R.; Nze, G. A.; Galvão, D.; Ribeiro, L. On the mechanical properties and fracture patterns of the nonbenzenoid carbon allotrope (biphenylene network): a reactive molecular dynamics study. *Nanoscale* **2022**, *14*, 3200−3211.
(15) Desyatkin, V. G.; Martin, W. B.; Aliev, A. E.; Chapman, N. E.; Fonseca, A. F.; Galvão, D. S.; Miller, E. R.; Stone, K. H.; Wang, Z.; Zakhidov, D.; Limpoco, F. T.; Almahdali, S. R.; Parker, S. M.; Baughman, R. H.; Rodionov, V. O. Scalable Synthesis and Characterization of Multilayer γ-Graphyne, New Carbon Crystals with a Small Direct Band Gap. *J. Am. Chem. Soc.* **2022**, *144*, 17999−18008.
(16) Aliev, A. E.; Guo, Y.; Fonseca, A. F.; Razal, J. M.; Wang, Z.; Galvão, D. S.; Bolding, C. M.; Chapman-Wilson, N. E.; Desyatkin, V. G.; Leisen, J. E.; Junior, L. A. R.; Kanegae, G. B.; Lynch, P.; Zhang, J.; Judicpa, M. A.; Parra, A. M.; Zhang, M.; Gao, E.; Hu, L.; Rodionov, V. O.; Baughman, R. H. A planar-sheet nongraphitic zero-bandgap sp^2 carbon phase made by the low-temperature reaction of γ-graphyne. *Proc. Natl. Acad. Sci. U.S.A.* **2025**, *122*, No. e2413194122.
(17) Li, Q.; Li, Y.; Chen, Y.; Wu, L.; Yang, C.; Cui, X. Synthesis of γ-graphyne by mechanochemistry and its electronic structure. *Carbon* **2018**, *136*, 248−254.
(18) Li, X.; Li, B.-h.; He, Y.-b.; Kang, F.-y. A review of graphynes: Properties, applications and synthesis. *New Carbon Mater.* **2020**, *35*, 619−629.
(19) Pereira Junior, M. L.; da Cunha, W. F.; Galvão, D. S.; Junior, L. A. R. A reactive molecular dynamics study on the mechanical properties of a recently synthesized amorphous carbon monolayer converted into a nanotube/nanoscroll. *Phys. Chem. Chem. Phys.* **2021**, *23*, 9089−9095.
(20) Felix, L. C.; Tromer, R. M.; Autreto, P. A.; Ribeiro Junior, L. A.; Galvao, D. S. On the mechanical properties and thermal stability of a recently synthesized monolayer amorphous carbon. *J. Phys. Chem. C* **2020**, *124*, 14855−14860.
(21) Hou, L.; Cui, X.; Guan, B.; Wang, S.; Li, R.; Liu, Y.; Zhu, D.; Zheng, J. Synthesis of a monolayer fullerene network. *Nature* **2022**, *606*, 507−510.
(22) Tromer, R. M.; Junior, L. A. R.; Galvão, D. S. A DFT study of the electronic, optical, and mechanical properties of a recently synthesized monolayer fullerene network. *Chem. Phys. Lett.* **2022**, *804*, No. 139925.
(23) Junior, L. R.; Junior, M. P.; Giozza, W.; Tromer, R.; Galvão, D. S. Thermal stability and fracture patterns of a recently synthesized monolayer fullerene network: A reactive molecular dynamics study. *Chem. Phys. Lett.* **2022**, *807*, No. 140075.
(24) Mortazavi, B.; Zhuang, X. Low and anisotropic tensile strength and thermal conductivity in the single-layer fullerene network predicted by machine-learning interatomic potentials. *Coatings* **2022**, *12*, 1171.
(25) Peng, B. Stability and Strength of Monolayer Polymeric C60. *Nano Lett.* **2023**, *23*, 652−658, DOI: 10.1021/acs.nanolett.2c04497.
(26) Loh, K. P. An old kid in the block: 2D polymeric C60. *Sci. China Mater.* **2022**, No. 836.
(27) Paupitz, R.; Fonseca, A. F.; Bessa, M.; Fabris, G. S.; da Cunha, W. F.; Machado, L. D.; Junior, M. P.; Junior, L. R.; Galvão, D. S. A concise review of recently synthesized 2d carbon allotropes: Amorphous carbon, graphynes, biphenylene and fullerene networks. *Carbon* **2026**, *252*, No. 121320.
(28) Wang, Y.; Zhang, K.; Zhao, Y.; Wu, Z.-H.; Zhou, Y.-Y.; Li, S.-L.; Wu, X.-Q.; Li, L.; Ke, C.; Xu, L.; Yi, J.-B.; Zhao, Y.; Long, J.-P.; Qiao, L. Comprehensive review of novel two-dimensional fullerene network: synthesis, theoretical investigations, and applications. *Rare Metals* **2025**, *44*, 9726−9746.
(29) Krachmalnicoff, A.; Bounds, R.; Mamone, S.; Alom, S.; Concistrè, M.; Meier, B.; Kouřil, K.; Light, M. E.; Johnson, M. R.; Rols, S.; Horsewill, A. J.; Shugai, A.; Nagel, U.; Rõõm, T.; Carravetta, M.; Levitt, M. H.; Whitby, R. J. The dipolar endofullerene HF@ C60. *Nat. Chem.* **2016**, *8*, 953−957.
(30) Dong, H.; Lin, B.; Gilmore, K.; Hou, T.; Lee, S.-T.; Li, Y. B40 fullerene: an efficient material for CO2 capture, storage and separation. *Curr. Appl. Phys.* **2015**, *15*, 1084−1089.
(31) Tan, W.; Yang, F.; Yi, T.; Liu, G.; Wei, X.; Long, Q.; Liu, Y.; Li, Y.; Guo, C.; Liu, K.; Lu, Z.; Liu, Q.; Xu, Z. Fullerene-like elastic carbon coatings on silicon nanoparticles by solvent controlled association of natural polyaromatic molecules as high-performance lithium-ion battery anodes. *Energy Storage Mater.* **2022**, *45*, 412−421.
(32) Shan, C.; Yen, H.-J.; Wu, K.; Lin, Q.; Zhou, M.; Guo, X.; Wu, D.; Zhang, H.; Wu, G.; Wang, H.-L. Functionalized fullerenes for highly efficient lithium ion storage: Structure-property-performance correlation with energy implications. *Nano Energy* **2017**, *40*, 327−335.
(33) Puente Santiago, A. R.; Fernandez-Delgado, O.; Gomez, A.; Ahsan, M. A.; Echegoyen, L. Fullerenes as key components for low-dimensional (photo) electrocatalytic nanohybrid materials. *Angew. Chem., Int. Ed.* **2021**, *60*, 122−141.
(34) Maroto, E. E.; Izquierdo, M.; Reboredo, S.; Marco-Martinez, J.; Filippone, S.; Martín, N. Chiral fullerenes from asymmetric catalysis. *Acc. Chem. Res.* **2014**, *47*, 2660−2670.
(35) Rapoport, L.; Fleischer, N.; Tenne, R. Fullerene-like WS2 nanoparticles: superior lubricants for harsh conditions. *Adv. Mater.* **2003**, *15*, 651−655.
(36) Rapoport, L.; Feldman, Y.; Homyonfer, M.; Cohen, H.; Sloan, J.; Hutchison, J.; Tenne, R. Inorganic fullerene-like material as additives to lubricants: structure−function relationship. *Wear* **1999**, *225*−*229*, 975−982.
(37) Shaikh, A.; Wu, J.; Peng, B. Negative and positive anisotropic thermal expansion in 2D fullerene networks. *Phys. Rev. Lett.* **2025**, *135*, No. 126103.
(38) Wang, R.; Li, H.; Shakoori, M. A.; Cheng, X.; Hu, Y.; Wang, L. Strain engineering of electronic structure and thermoelectric properties of quasi-hexagonal fullerene monolayer. *J. Appl. Phys.* **2024**, *136*, No. 015101.
(39) Wang, R.-P.; Yu, T.-T.; Shakoori, M. A.; Han, M.-J.; Hu, Y.-X.; Tang, H.-K.; Li, H.-P. Phonon Thermal Transport at Interfaces of Graphene/Quasi-Hexagonal Phase Fullerene Heterostructure. *Chin. Phys. Lett.* **2025**, *42*, No. 046601.
(40) Cassiano, T. S. A.; Pereira, M.; e Silva, G.; de Oliveira Neto, P. H.; Ribeiro, L. Large polarons in two-dimensional fullerene networks: the crucial role of anisotropy in charge transport. *Nanoscale* **2024**, *16*, 2337−2346.
(41) Ren, Y.; Lu, Y.; Zhang, D. Enhanced hydrogen storage capacity in two-dimensional fullerene networks. *J. Phys. Chem. Lett.* **2023**, *14*, 11051−11057.
(42) Gonzalez, M.; Lujan, S.; Beran, K. A. Investigation into the molecular structure, electronic properties, and energetic stability of endohedral (TM@ C20) and exohedral (TM-C20) metallofullerene derivatives of C20: TM= Group 11 and 12 transition metal atoms/ions. *Comput. Theor. Chem.* **2017**, *1119*, 32−44.
(43) Lu, X.; Feng, L.; Akasaka, T.; Nagase, S. Current status and future developments of endohedral metallofullerenes. *Chem. Soc. Rev.* **2012**, *41*, 7723−7760.
(44) Wu, Y.; Zhou, Z.; Wang, Z. Stability and Electronic Properties of 1D and 2D Ca@ C60 Oligomers and Polymers. *Inorganics* **2024**, *12*, 45.
(45) Zhao, Y.; Guo, Y.; Zhao, Y.; Yu, X.; Cherenda, N.; Su, Y.; Zhao, J. Two-dimensional fullerene-based monolayer materials assembled by C80 and Sc3N@ C80. *Phys. Chem. Chem. Phys.* **2024**, *26*, 10841−10849, DOI: 10.1039/D3CP04028C.
(46) Levitt, M. H. Spectroscopy of light-molecule endofullerenes. *Philos. Trans. R. Soc., A* **2013**, *371*, No. 20120429.

https://doi.org/10.1021/acs.jpcc.6c02579
J. Phys. Chem. C 2026, 130, 7900−7908

(47) Pacheco, J. M.; Gueorguiev, G.; Martins, J. L. First-principles study of the possibility of condensed phases of endohedral silicon cage clusters. *Phys. Rev. B* **2002**, *66*, No. 033401.
(48) Oliveira, M. J. T.; Medeiros, P. V.; Sousa, J. R.; Nogueira, F.; Gueorguiev, G. K. Optical and magnetic excitations of metal-encapsulating Si cages: A systematic study by time-dependent density functional theory. *J. Phys. Chem. C* **2014**, *118*, 11377−11384.
(49) Murata, M.; Murata, Y.; Komatsu, K. Synthesis and properties of endohedral C60 encapsulating molecular hydrogen. *J. Am. Chem. Soc.* **2006**, *128*, 8024−8033.
(50) Pei, C.; Wang, L. Recent progress on high-pressure and high-temperature studies of fullerenes and related materials. *Matter Radiat. Extremes* **2019**, *4*, No. 028201.
(51) Hoffman, G.; Walkey, M. C.; Gräsvik, J.; Bacanu, G. R.; Alom, S.; Bloodworth, S.; Light, M. E.; Levitt, M. H.; Whitby, R. J. A Solid-State Intramolecular Wittig Reaction Enables Efficient Synthesis of Endofullerenes Including Ne@ C60, 3He@ C60, and HD@ C60. *Angew. Chem., Int. Ed.* **2021**, *60*, 8960−8966.
(52) López-Alcalá, D.; Hu, Z.; Baldoví, J. J. Graphendofullerene: a novel molecular two-dimensional ferromagnet. *Chem. Sci.* **2025**, *16*, 7659−7666.
(53) Zhao, X.-K.; Zhao, J.; Wei, S.-R.; Qiu, Y.-Z.; He, Y.; Hu, H.-S.; Li, J. A design strategy for single-molecule magnet materials with fullerene confinement-induced unpaired f-electrons. *Chem. Sci.* **2025**, *16*, 12087−12095, DOI: 10.1039/D5SC01607J.
(54) Martínez-Flores, C.; Basiuk, V. A. Ln@C60 endohedral fullerenes: A DFT analysis for the complete series from lanthanum to lutetium. *Comput. Theor. Chem.* **2022**, *1217*, No. 113878.
(55) Basiuk, V. A. Electron smearing in DFT calculations: A case study of doxorubicin interaction with single-walled carbon nanotubes. *Int. J. Quantum Chem.* **2011**, *111*, 4197−4205.
(56) Renzler, M.; Kranabetter, L.; Goulart, M.; Scheier, P.; Echt, O. Positively and Negatively Charged Cesium and (C60) m Cs n Cluster Ions. *J. Phys. Chem. C* **2017**, *121*, 10817−10823.
(57) Rose, H. R.; Dance, I. G.; Fisher, K. J.; Smith, D. R.; Willett, G. D.; Wilson, M. A. Endohedral barium and strontium fullerenes. *J. Chem. Soc., Chem. Commun.* **1993**, 1361−1363.
(58) Gao, F.; Zhao, G.-L.; Yang, S.; Spivey, J. J. Nitrogen-doped fullerene as a potential catalyst for hydrogen fuel cells. *J. Am. Chem. Soc.* **2013**, *135*, 3315−3318.
(59) Dion, M.; Rydberg, H.; Schröder, E.; Langreth, D. C.; Lundqvist, B. I. Van der Waals Density Functional for General Geometries. *Phys. Rev. Lett.* **2004**, *92*, No. 246401.
(60) Thonhauser, T.; Cooper, V. R.; Li, S.; Puzder, A.; Hyldgaard, P.; Langreth, D. C. Van der Waals density functional: Self-consistent potential and the nature of the van der Waals bond. *Phys. Rev. B* **2007**, *76*, No. 125112.
(61) Román-Pérez, G.; Soler, J. M. Efficient Implementation of a van der Waals Density Functional: Application to Double-Wall Carbon Nanotubes. *Phys. Rev. Lett.* **2009**, *103*, No. 096102.
(62) Soler, J. M.; Artacho, E.; Gale, J. D.; García, A.; Junquera, J.; Ordejón, P.; Sánchez-Portal, D. The SIESTA method for ab initio order-N materials simulation. *J. Phys.: Condens. Matter* **2002**, *14*, 2745.
(63) Basiuk, V. A.; Prezhdo, O. V.; Basiuk, E. V. Thermal smearing in DFT calculations: How small is really small? A case of La and Lu atoms adsorbed on graphene. *Mater. Today Commun.* **2020**, *25*, No. 101595.
(64) Perdew, J. P.; Burke, K.; Ernzerhof, M. Generalized gradient approximation made simple. *Phys. Rev. Lett.* **1996**, *77*, 3865.
(65) Ernzerhof, M.; Scuseria, G. E. Assessment of the Perdew-Burke-Ernzerhof exchange-correlation functional. *J. Chem. Phys.* **1999**, *110*, 5029−5036.
(66) Troullier, N.; Martins, J. L. Efficient pseudopotentials for plane-wave calculations. *Phys. Rev. B* **1991**, *43*, 1993.
(67) Fadaie, M.; Shahtahmassebi, N.; Roknabad, M. R. Effect of external electric field on the electronic structure and optical properties of stanene. *Opt. Quantum Electron.* **2016**, *48*, No. 440.
(68) Tignon, J.; Voisin, P.; Delalande, C.; Voos, M.; Houdré, R.; Oesterle, U.; Stanley, R. P. From Fermi's Golden Rule to the Vacuum Rabi Splitting: Magnetopolaritons in a Semiconductor Optical Microcavity. *Phys. Rev. Lett.* **1995**, *74*, 3967−3970.
(69) Silveirinha, M. G. Examining the validity of Kramers-Kronig relations for the magnetic permeability. *Phys. Rev. B* **2011**, *83*, No. 165119.
(70) Chatterjee, A.; Biswas, A.; Fuhr, A. S.; Terlier, T.; Sumpter, B. G.; Ajayan, P. M.; Aharonovich, I.; Huang, S. Room-temperature high-purity single-photon emission from carbon-doped boron nitride thin films. *Sci. Adv.* **2025**, *11*, No. eadv2899.
(71) Xu, J.; Liang, Q.; Li, Z.; Osipov, V. Y.; Lin, Y.; Ge, B.; Xu, Q.; Zhu, J.; Bi, H. Rational Synthesis of Solid-State Ultraviolet B Emitting Carbon Dots via Acetic Acid-Promoted Fractions of sp3 Bonding Strategy. *Adv. Mater.* **2022**, *34*, No. 2200011.

https://doi.org/10.1021/acs.jpcc.6c02579
J. Phys. Chem. C 2026, 130, 7900−7908